ACS APPLIED NANO MATERIALS

www.acsanm.org Article

Z-Contrast Enhancement in Au−Pt Nanocatalysts by Correlative X-ray Absorption Spectroscopy and Electron Microscopy: Implications for Composition Determination

Yang Liu,[#] Maichong Xie,[#] Nicholas Marcella, Alexandre C. Foucher, Eric A. Stach, Marc R. Knecht,* and Anatoly I. Frenkel*

Cite This: *ACS Appl. Nano Mater.* 2022, 5, 8775−8782 Read Online

ABSTRACT: The properties of bimetallic nanoparticles (BNPs) vary widely as a function of their composition and size distributions. X-ray absorption fine structure analysis is commonly used to characterize their structure, but its application to elements that are close to each other in the periodic table is hampered by poor Z-contrast. We trained an artificial neural network to recognize the partial coordination numbers in AuPt NPs synthesized via peptide templating using their X-ray absorption near-edge structure spectra. This approach, combined with scanning transmission electron microscopy analysis, revealed unique details of this prototype catalytic system that has different forms of heterogeneities at both the intra- and inter-particle levels. Our method based on the enhancement of Z-contrast of metal species will have implications for compositional studies of BNPs.

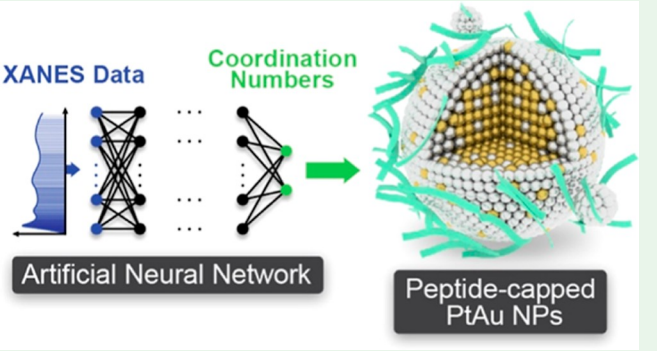

KEYWORDS: *nanoparticles, peptides, XANES, machine learning, neural network, STEM*

INTRODUCTION

Bimetallic nanoparticles (BNPs) have received tremendous attention due to their use in many biomedical, mechanical, pharmaceutical, catalytic, and electrocatalytic applications.[1] For example, due to their diverse architectural and compositional motifs that can be tuned by design,[2−5] many types of catalytic BNPs have been reported.[5,6] In order to rationally design BNPs with the desired performance, a descriptor-based approach is being increasingly adopted. With this approach, structural, electronic, and chemical properties are parameterized, and their relationship with the BNP performance is determined.[7,8] A convenient strategy toward understanding structural and compositional properties of the BNPs is to measure their metal−metal coordination numbers (CNs) and use them to estimate the average size and compositional habits (e.g., distinguish between core−shell and random alloys).[9,10] In a typical research program, such information is extracted from an extended X-ray absorption fine structure (EXAFS) experiment, where absorption edges of each A_xB_{100-x} alloy component, A and B, can be independently measured and analyzed to obtain the partial CNs: N_{A-A} and N_{A-B} (for the A absorption edge) and N_{B-A} and N_{B-B} (for the B absorption edge).

While EXAFS can be readily applied to most BNPs of interest, there is an important class of these structures that contains elements that cannot be easily distinguished. This occurs when the two metals in the BNP are too close in the same row of the periodic table (e.g., Pt−Au, Pt−Ir, Cu−Ni, Ag−Pd, etc.). This occurs due to the sensitivity of EXAFS, which cannot discriminate between the backscattering (A or B) species for A−B and A−A pairs (or B−A and B−B pairs) if A and B have similar Z numbers. To further complicate matters, the absorption edges of the nearby elements in the same row of the periodic table often overlap, so that large portions of the EXAFS signals from both edges (e.g., Pt and Au[9] or Pt and Ir L_3-edges[11] or As K-edge and Au L_3-edge[12]) coexist in the same energy range. One development[9,11] is noteworthy, wherein simultaneous EXAFS analysis of overlapping edges was used to disentangle competing contributions from both edges. However, this requires that effective A−M and B−M (where M = A or B) CNs can be obtained, not partial ones, hence limiting an ability to perform detailed compositional analyses.[13]

An attractive alternative approach is to extract CNs from X-ray absorption near-edge spectroscopy (XANES) and not from

Received: January 25, 2022
Accepted: June 6, 2022
Published: June 21, 2022

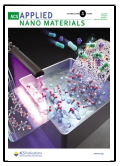

https://doi.org/10.1021/acsanm.2c00393
ACS Appl. Nano Mater. 2022, 5, 8775−8782

EXAFS itself. The near-edge region of each element's absorption edge has unique sensitivity to the charge state of that element, which may change because of alloying. Thus, if the XANES spectrum measured for an absorption edge of element A can be related to the numbers of A−A and A−B pairs in the nearest neighboring environment, it would result in the same information that cannot be determined by EXAFS. Due to the lack of analytical methods for recovering the partial CNs from XANES, a machine learning (ML) method was recently developed for this purpose. It was shown by us and others that the ML approach can map XANES spectra onto structural descriptors for monometallic,[14,15] bimetallic,[16,17] and metal oxide systems[18] as well as other applications.[19−21] In addition to being a very good alternative to EXAFS, the ML-XANES method stands out as the only tool for analysis of catalysts under operando conditions, in the liquid phase, or when exposed to high temperature and pressure. In such systems EXAFS data are either of poor quality or unavailable. While ML-XANES has been exceedingly helpful in rapid analysis of BNPs under extreme conditions, it has never been used, to the best of our knowledge, for studying BNPs with elements that have poor Z-contrast. Such an approach could prove to be transformational and allow for atomically resolved analyses of an important class of materials, such as nanocatalysts, for which no readily accessible technique other than—as we show directly here—scanning transmission electron microscopy (STEM)−energy-dispersive spectroscopy (EDS) is available to confirm the atomic arrangement of the metal species.

We have chosen peptide-capped PtAu BNPs for this study based upon their wide range of potential applications.[22,23] To fabricate the BNPs in water, a multistep coreduction process was developed to generate the final materials. They were passivated on the surface using the AuBP2 peptide (WALRRSIRRQSY), previously identified with an affinity for Au.[24] Each step in the process was monitored to identify the effects of the reaction on the synthesis of the bimetallic structures. Once prepared, the BNPs were examined using the ML-XANES-based approach, which allowed for the resolution of the partial CN values of Pt and Au, which could not be achieved via conventional EXAFS analysis. The results demonstrated that a nonalloyed system was generated with a cluster-in-cluster morphology. In addition, separate monometallic Pt NPs were present in the reaction mixture, which was confirmed with high-resolution STEM−EDS analysis. Such results demonstrate that advanced characterization with atomic resolution is possible for structures not accessible via conventional approaches. Such ML-XANES methods could be adapted for a variety of systems, including in situ analysis, thus advancing knowledge of fundamental structure−property relationships that cannot be presently addressed.

RESULTS AND DISCUSSION

The synthesis procedure developed for AuPt NPs is described in the Materials and Methods section and shown in Scheme 1. For this, K_2PtCl_4 and AuBP2 peptide were comixed in water for 72 h for Pt^{2+} hydrolysis that was required for metal ion binding to the peptide, which was monitored using UV−vis spectroscopy (Figure 1). The spectra (Figure 1a) of the materials prepared at the anticipated Pt/Au ratios are shown immediately after solution production (time = 0 h). For this system, $PtCl_4^{2-}$ ligand-to-metal charge transfer (LMCT) bands were observed at 215 and 230 nm,[25] where their intensity was directly proportional to the amount of Pt^{2+} in the mixture. Over time

Scheme 1. Synthesis Procedure of the AuBP2-Capped Pt−Au NPs

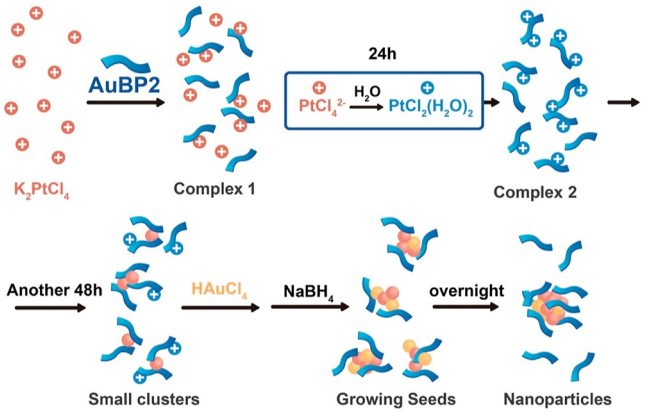

(Figure 1b−d), the intensity of these peaks decreased, and the growth of two new peaks at 250 and 305 nm was evident. As anticipated, the intensity of these new bands, which is consistent with the coordination of Pt^{2+} to the peptide amines,[25,26] was directly proportional to the amount of Pt in the system. Figure 1e shows the intensity of the 250 nm peak as a function of time and Pt^{2+} concentration, confirming continued growth of the absorbance over the 72 h reaction. Such studies were consistent with the prior results for dendrimer-encapsulated NPs (DENs), where similar reactivity was noted.[26]

Beyond the LMCT bands associated with the Pt^{2+} ions, two additional points of interest are observed in the UV−vis analysis of Figure 1. For this, however, it is important to note that all of the spectra are background subtracted against the peptide at the reaction concentration. First, two noticeable troughs in the spectra were evident at 225 and 280 nm. For the 225 nm region, the spectra even became negative, suggesting that changes are likely from the peptide itself. Second, over time, a broad increase in absorbance toward lower wavelengths was observed for the sample that is directly proportional to the Pt concentration in the reaction. Taken together, this suggests that the peptide potentially reduces a fraction of the Pt^{2+} ions to Pt^0. For the first point, spectral troughs at 225 and 280 nm likely arise from oxidation of the tryptophan residues of the AuBP2 peptide, which drive the Pt^{2+} reduction. Tryptophan is known to reduce metal ions in solution, where it is oxidized to kynurenine.[27,28] Tyrosine has also been shown to have the ability to reduce metal ions,[29,30] potentially facilitating these observed spectral changes and the production of Pt^0.[31] Once Pt^{2+} is reduced to Pt^0, the nucleation of small Pt^0 clusters is likely, leading to NP growth, giving rise to the broad absorbance noted in the second point.[32]

After 72 h of hydrolysis, sufficient Au^{3+} was added to the Pt^{2+}/peptide system to achieve the appropriate Pt/Au ratios. The materials were then reduced with excess $NaBH_4$, generating the stable BNP colloidal suspension. Figure 1f shows the UV−vis spectra of the reduced materials. For all the Pt-containing materials, a broad absorbance band was noted that increased in absorbance toward lower wavelengths, consistent with the formation of BNPs. For the Pt_0Au_{100} sample (i.e., monometallic Au), a plasmon band centered at 530 nm was also observed. Such studies are all fully consistent with NP formation. It is interesting to point out, however, that the Pt−N LMCT band remains present in the BNP samples. This suggests that the Pt−N interaction remains after reduction, which could arise from

https://doi.org/10.1021/acsanm.2c00393
ACS Appl. Nano Mater. 2022, 5, 8775−8782

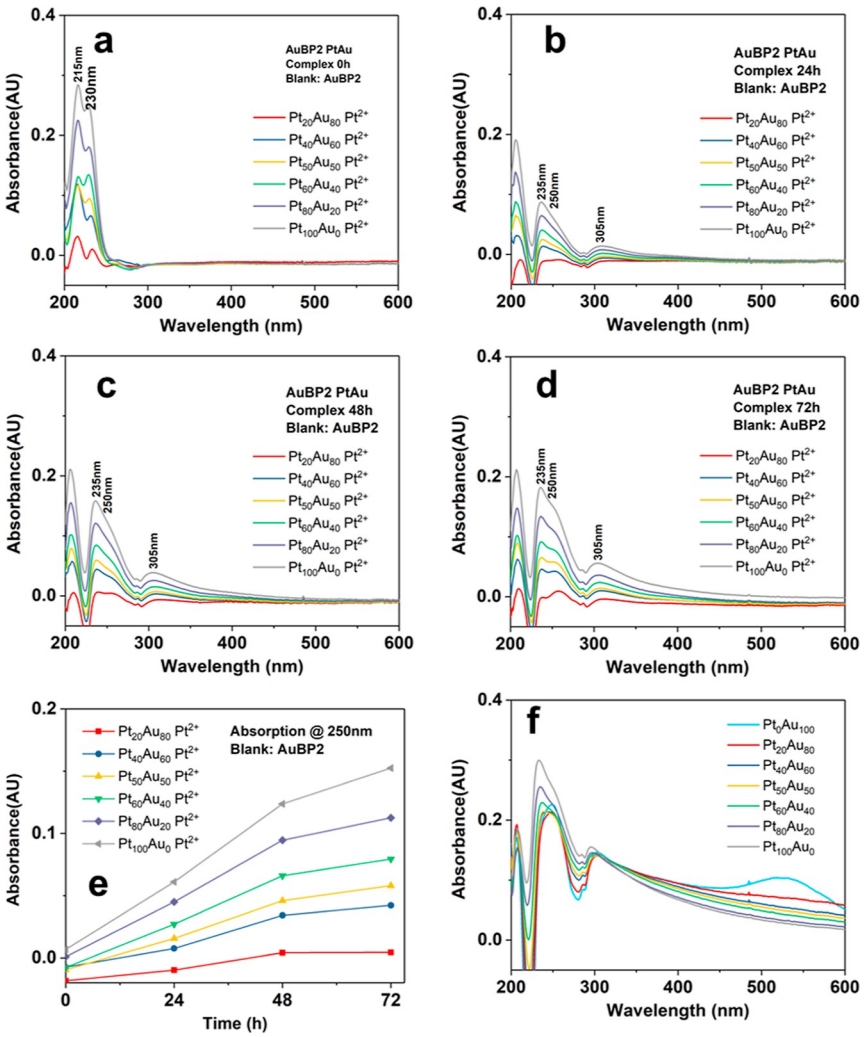

Figure 1. UV−vis analysis of the AuBP2−Pt^{2+} complex at (a) 0, (b) 24, (c) 48, and (d) 72 h. (e) Full set of AuBP2−Pt^{2+} complex absorption at 250 nm during the 72 h hydrolysis and (f) UV−vis analysis of the reduced BNPs capped with AuBP2.

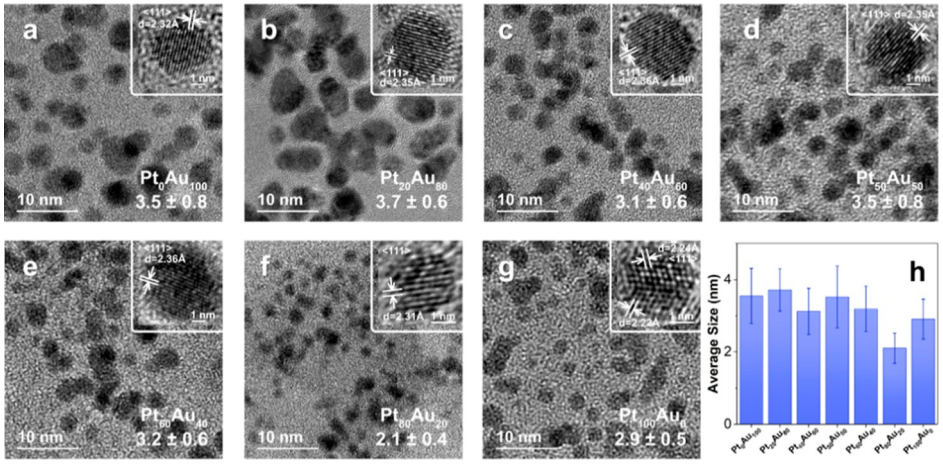

Figure 2. HR-TEM analysis of colloidal PtAu BNPs capped by AuBP2: (a) Pt_0Au_{100}, (b) $Pt_{20}Au_{80}$, (c) $Pt_{40}Au_{60}$, (d) $Pt_{50}Au_{50}$, (e) $Pt_{60}Au_{40}$, (f) $Pt_{80}Au_{20}$, and (g) $Pt_{100}Au_0$. (h) Average BNP sizes of the indicated compositions.

the peptide binding to the BNP surface or potentially from a fraction of the Pt^{2+}−peptide complex that remains unreduced.

To confirm that NP production occurred, high-resolution TEM (HR-TEM) analysis of the peptide-capped BNPs was performed (Figures 2 and S1). For all the samples, the NPs were approximately spherical in shape and ranged in size from 2.1 ± 0.4 nm for the $Pt_{80}Au_{20}$ sample to 3.7 ± 0.6 nm for the $Pt_{20}Au_{80}$ system. Analysis of more than 100 individual NPs was performed to identify average particle sizes. Lattice-resolved images for each sample, shown in the insets, confirmed that

https://doi.org/10.1021/acsanm.2c00393
ACS Appl. Nano Mater. 2022, 5, 8775−8782

crystalline materials were prepared. No trends between changes in metallic composition and particle size were evident (Figure 2h).

XAFS measurements were performed at the ISS (8-ID) beamline of the National Synchrotron Light Source-II (NSLS-II) at the Brookhaven National Laboratory. The solution samples were sealed in Kapton tubes with an ~5 mm inner diameter and a wall thickness of 0.2 mm. For each sample, 50 scans were collected to improve the data quality. Three samples with different ratios ($Pt_{80}Au_{20}$, $Pt_{60}Au_{40}$, and $Pt_{20}A_{80}$) were measured at both the Au L_3-edge and Pt L_3-edge. The experimental data are shown in Figure 3. At the Au L_3-edge,

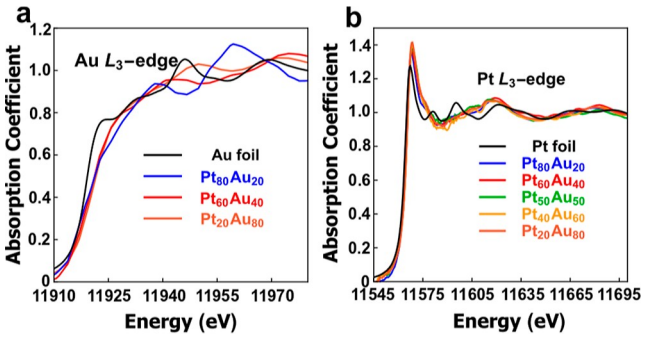

Figure 3. XANES data of $Pt_{100-x}Au_x$ BNPs at (a) Au and (b) Pt L_3-edges.

there are peak intensity and position changes in the near-edge region which are correlated with different Au/Pt ratios; however, at the Pt L_3-edge, the changes are much weaker.

To quantitatively analyze the experimental XANES data and to obtain information about partial CNs of Pt- and Au-absorbing atoms, the neural network (NN) approach was applied. Detailed information regarding the method is described in the Materials and Methods section. Similar to our previous work where we correlated the XANES spectrum with the structural descriptors of Pt and AuPd NPs,[14,16] the NN was constructed to build a correlation between the XANES spectrum and structural descriptors: Au−Au, Au−Pt, Pt−Au, and Pt−Pt CNs. To train the NN, a large dataset is required to get a good performance. Here, we exploited theoretical approaches [FEFF[33] and finite difference method near-edge structure (FDMNES[34])] to construct the training dataset. The standard Au and Pt foils were simulated initially to provide optimized parameters, which are shown in Supporting Information, Figure S3. Then, the AuPt atomistic models were constructed based on similar structures and with Au/Pt ratios ranging from 1:9 to 9:1, which covers the composition range of the experimental XANES measurements. To account for the changes in lattice parameters with alloy composition, Vegard's law was used. The effective lattice constants ranged from 3.92 to 4.07 Å (i.e., spanning the range between pure Pt and Au). From this analysis, there were 6578 sites of AuPt atomistic models at the Pt L_3-edge and 8159 sites of AuPt models at the Au L_3-edge calculated through FEFF and FDMNES. The sites are the different absorbing atoms. In addition, a linear combination approach was employed to enlarge the dataset, as described in our previous study.[14] Using this approach, 100,000 spectra were prepared and randomly shuffled as the total dataset, which was split into an 8:1:1 ratio as the training dataset: validation dataset: test dataset. Here, the training dataset worked as the major dataset to optimize the parameters in the NN. The validation dataset worked as a benchmark to evaluate the training performance of each training epoch and was used to help optimize the hyperparameters of the NN. The final NN structure is illustrated in Table S1.

To validate the NN and evaluate its performance, a test dataset was exploited (Figure 4). The error estimation in the NN

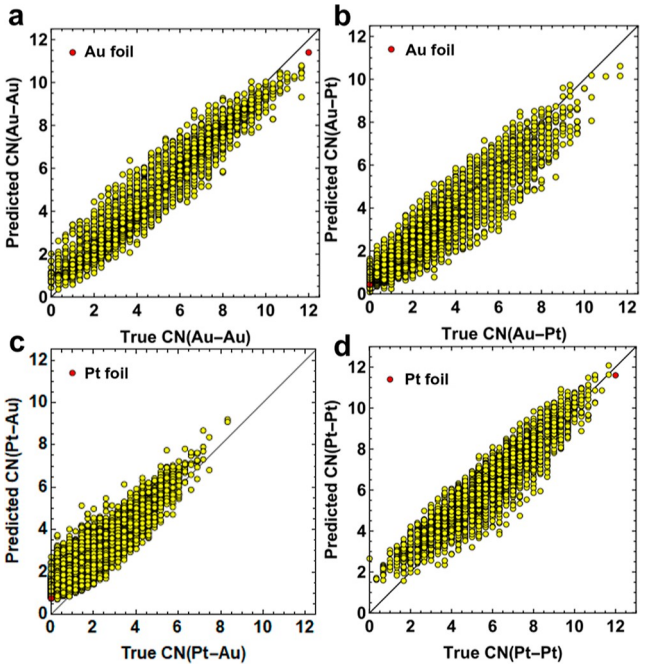

Figure 4. Validation of the NN using the predicted (a) CN_{Au-Au}, (b) CN_{Au-Pt}, (c) CN_{Pt-Au}, and (d) CN_{Pt-Pt} vs true values.

models is given in Supporting Information, Section S1. After the NN validation with the test dataset, it was applied to evaluate the experimental XANES spectra. The results for the predicted CNs of Pt−Au, Pt−Pt, Au−Au, and Au−Pt first nearest neighboring pairs are summarized in Table 1. Using these results, the molar fraction of Au atoms, x_{Au}, was calculated to be equal to $CN_{Pt-Au}/(CN_{Au-Pt} + CN_{Pt-Au})$.[13] Using the obtained value of x_{Au}, the Cowley short-range order (SRO) parameter was calculated using the equation given below[13,35]

$$\alpha = 1 - \frac{CN_{Pt-Au}/(CN_{Pt-Au} + CN_{Pt-Pt})}{x_{Au}}$$

When the average A−M and B−M CN values are similar, the distribution of elements within the BNPs is considered to be homogeneous; however, if the SRO parameter is positive or negative, it indicates either a positive or negative tendency, respectively, to clustering of like atoms. If the SRO parameter is 0, it indicates a random alloy.[35] In the present case, however, the results for CN_{Pt-Pt} (Table 1) are intriguing because they change relatively weakly with composition (also evident in the raw data behavior, Figure 3b), while CN_{Au-Au} values exhibit strong changes. Furthermore, the large Pt−Pt CN values for all compositions (close to 11−12) appear to be inconsistent with a model of a representative BNP with Pt and Au atoms coexisting in the same particle. This suggests that the distribution of Pt within the sample was bimodal, where some Pt atoms segregate in a separate phase from the PtAu-alloyed NPs.

To test this hypothesis and to further validate the ML-XANES analysis results, the high-angle annular dark-field (HAADF)−STEM and EDS analyses were employed to characterize the

https://doi.org/10.1021/acsanm.2c00393
ACS Appl. Nano Mater. 2022, 5, 8775−8782

Table 1. NN Analysis Results of the XANES Data at the Au L_3-Edge and Pt L_3-Edge

sample	CN_{Pt-Au}	CN_{Pt-Pt}	CN_{Au-Au}	CN_{Au-Pt}	x_{Au}	α	CN_{M-M}
$Pt_{20}Au_{80}$	1.1 ± 0.8	11.3 ± 0.6	7.8 ± 0.5	0.8 ± 0.6	0.57	0.85	10.2
$Pt_{40}Au_{60}$	1.2 ± 0.8	11.7 ± 0.6	5.6 ± 0.4	0.6 ± 0.6	0.67	0.86	8.4
$Pt_{80}Au_{20}$	1.1 ± 0.8	12.0 ± 0.6	0.6 ± 0.5	6.4 ± 0.6	0.15	0.43	12.0

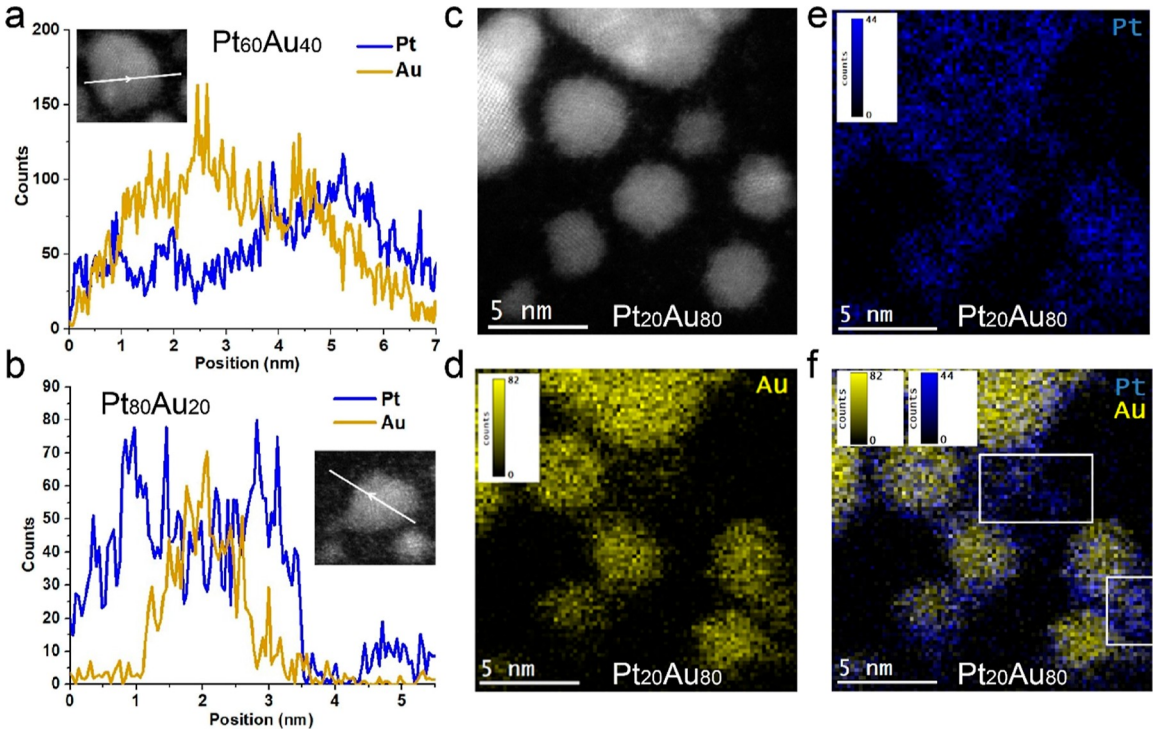

Figure 5. HAADF−STEM images and EDS line scan of AuBP2-capped (a) $Pt_{60}Au_{40}$ and (b) $Pt_{80}Au_{20}$ BNPs. For (a), the first half of the BNP is Au-rich, while the second half is Pt-rich. The scan is evidence of compositional heterogeneities within the particles. (c−f) HAADF−STEM images and EDS mappings of AuBP2-capped $Pt_{20}Au_{80}$ NPs.

distribution of Au and Pt atoms in three samples: $Pt_{80}Au_{20}$, $Pt_{60}Au_{40}$, and $Pt_{20}Au_{80}$. The results are summarized in Figures 5 and S5−S8 of the Supporting Information. STEM analysis of the samples showed an increased presence of isolated atoms when the Pt concentration was increased. In Figure 5, scattered atoms are visible around $Pt_{20}Au_{80}$. The EDS spectrum for a region containing only isolated atoms in the $Pt_{20}Au_{80}$ samples showed that these scattered atoms are mostly Pt, although a minor fraction of Au atoms was also detected (Figure 5). It is important to note that inductively coupled plasma−mass spectroscopy (ICP−MS) analysis was performed on the sample, where the values obtained generally reflected the ratio of Pt/Au added to the sample.

EDS maps and line scans were measured to visualize the distribution of elements within the tested particles. In all BNP samples studied, a core−shell configuration was observed for most particles, with Pt segregated on the surface (Figure 5). Additionally, line scans showed the presence of compositional heterogeneity within the particles. In Figure 5a, it is possible to distinguish a Au-rich region on one side of a particle and a Pt-rich region on the other side, which is the evidence of a heterogeneous distribution of the alloyed and unalloyed structures.

The ability to discern between different models of the local structure depends critically on the combination of the ensemble-average information obtained by XAFS and local statistical information, such as that obtained by STEM−EDS. Without the latter, there are too many possible interpretations of the former when inner particle heterogeneities are present, as we and others have demonstrated earlier.[36−41] By combining the information from the EDS mapping and the XANES data, it becomes evident that a bimodal distribution of Pt is present. With more Pt loaded into the sample, a thicker Pt shell structure and isolated Pt particles were observed as shown in Figures 5 and S6−S7 for samples of $Pt_{20}Au_{80}$, $Pt_{60}Au_{40}$, and $Pt_{80}tAu_{20}$. Additional STEM images and EDS spectra in Figures S8−S10 also reveal the Pt shell structure with more Au in the core. This effect leads to high CN_{Pt-Pt} values and a negligible change in the Pt−Au CNs, as determined by NN-XANES. At the same time, a bimetallic core existed as a heterogeneous Pt−Au alloy with a limited amount of Pt atoms (since even with a larger Pt loading, some of them keep contributing to the shell structure and some to the separate Pt particles), which explained why CN_{Au-Au} decreased with a lower Au loading. Thus, the correlation between the changes in CN_{Au-Au} and CN_{Au-Pt} indicates that Au atoms were predominantly distributed in the BNP cores; the relatively unchanged and large CN_{Pt-Pt} values indicate a Pt-rich shell and/or coexisting Pt-rich NPs, which are both observed by EDS mapping. However, due to the limited statistics of EDS mapping, we cannot generalize the observed core−shell motif as the general properties of the entire samples. Supporting Information Figures 11−13 show good overall agreement with the trends obtained by the ML-XANES analysis. Indeed, from the Au atoms perspective, they are predominantly colocalized with Pt,

https://doi.org/10.1021/acsanm.2c00393
ACS Appl. Nano Mater. 2022, 5, 8775−8782

and thus, their CNs are sensitive to the Au/Pt ratios (Table 1). Specifically, the CN of Au−Pt increases when the Au/Pt ratio decreases (Table 1). This observation is consistent with the trends shown in Figures S11−S13. Indeed, as the Pt/Au ratio decreases (from 80:20 to 60:40 to 20:80), the relative amount of Pt in the bimetallic NP region decreases (as evident in Supporting Information, Figures 11−13, respectively), in agreement with the change in ML-XANES-determined CNs of AuPt (Table 1).

This bimodal distribution of Pt likely formed due to two reasons: the peptide-driven reduction of Pt^{2+} and the different reduction potentials of Pt and Au ions employed in the reaction. In the first situation, a fraction of the Pt^{2+} ions were prereduced by the peptide prior to the addition of Au^{3+}. This likely gives rise to the monometallic Pt particles observed in the samples. In the second situation, Au^{3+} is easier to reduce than Pt^{2+} due to differences in their reduction potentials.[42] In addition, the Pt^{2+} species were coordinated to the peptide, while the Au^{3+} ions were expected to be free in solution. These differences in the reduction potential and local environment could facilitate more rapid reduction of Au^{3+} over Pt^{2+} to give rise to the Au-rich core that is then decorated on the surface with the Pt shell upon Pt^{2+} reduction. While electron microscopy analysis provides illustration of such heterogeneous structures at the local scale of individual NPs, the Z-contrast of XANES— which was traditionally limited to PtAu (and other alloys with neighboring elements) but is now enhanced by the application of the NN approach—can also provide information regarding heterogeneity at the scale of the entire ensemble. The combination of NN-XANES and quantitative STEM for this class of BNPs and other heterogeneous nanostructures enables understanding of complex compositional distributions at both the intra- and interparticle levels.

CONCLUSIONS

In summary, combined correlative NN−XANES and HAADF−STEM analysis of peptide-capped BNPs containing neighboring elements such as Pt and Au was used to obtain elusive structural descriptors that helped elucidate the structural and compositional changes caused by different ratios of Au/Pt. A bimodal distribution of Pt was discovered with the coexistence of AuPt and Pt particles. This method will provide a general solution to a long-standing problem of analysis of the structure of other bimetallic nanocatalysts with overlapping absorption energy edges (e.g., Pt−Au, Pt−Ir, Cu−Ni, Ag−Pd, etc.).

MATERIALS AND METHODS

Synthetic Approach for the AuPt NPs with Peptide. Production of the peptide-capped PtAu NPs was initially attempted through the direct reduction of $HAuCl_4$ and K_2PtCl_4 in the presence of the AuBP2 peptide. The Pt/Au ratio was varied to control the final composition of the materials, where the different materials are denoted by Pt_xAu_{100-x}; however, upon reduction with $NaBH_4$, rapid precipitation of the bulk material was observed. Prior studies using DENs suggested that the hydrolysis of the $PtCl_4^{2-}$ ion to $PtCl_2(H_2O)_2^{2-}$ was required for complexation to amines of the polymeric template.[2] Since similar events were anticipated using the AuBP2 peptide, the hydrolysis of the Pt^{2+} salt was studied for BNP formation. For this, K_2PtCl_4 was mixed with the AuBP2 peptide in water at selected ratios for 72 h for all syntheses. Using this approach resulted in the production of highly stable peptide-capped BNPs. The AuBP2-capped bimetallic PtAu NPs were synthesized following a modified coreduction-based method. Seven different NPs were prepared at selected Pt/Au ratios of 0:100, 20:80, 40:60, 50:50, 60:40, 80:20, and 100:0. The description of the synthesis of the $Pt_{50}Au_{50}$ sample is provided; however, identical methods were employed to prepare all of the samples but with changes in the amount of metal ion salt solutions added to the reaction. Briefly, 1 mL of an aqueous 1 mM AuBP2 solution was diluted with 3.96 mL of water. To this mixture, 5 μL of a 100 mM K_2PtCl_4 solution in water was added. The Pt^{2+}/AuBP2 solution was then allowed to stir on a benchtop for 3 days at room temperature. Once complete, 5 μL of an aqueous 100 mM $HAuCl_4$ solution was added to the reaction. After a 15 min incubation time, 30 μL of freshly prepared 100 mM $NaBH_4$ was added to reduce the metal ions overnight. In all reactions, the ratio of total metal loading/AuBP2/$NaBH_4$ remained 1:1:3.

UV−Vis, TEM, and STEM Analyses. UV−vis analyses were conducted on an Agilent 8453 spectrophotometer using a 1 cm quartz cuvette. HR-TEM samples were prepared by drop-casting 5 μL of the NP solution onto a carbon-coated copper TEM grid, which was allowed to dry in a desiccator. TEM images were obtained using a Tecnai F30 (FEI) instrument operating at 300 kV. Analysis of >100 individual NPs was used to identify average particle sizes. STEM was performed with a JEOL NEOARM operating at 200 kV. The used probe current was 150 pA, with a camera length of 4 cm and a condenser lens aperture size of 40 μm. This leads to a convergence angle of approximately 27 mrad. EDS data were collected with two integrated detectors provided by JEOL. They have a collection angle of 0.97 sr. All STEM images were taken right before EDS acquisition. HAADF images were collected with a Gatan Inc. detector. The samples prepared for STEM analysis were all free-standing particles and directly deposited on the carbon film. A drop of solution was deposited on a carbon-coated copper TEM grid from Electron Microscopy Science.

XRD Analysis. Powder XRD analyses were conducted using a Bruker D8 ADVANCE powder X-ray diffractometer with DAVINCI design and a LYNXEYE high-speed 1-D detector. To obtain the necessary NP powder, all samples were lyophilized to remove the water solvent. The XRD result is shown in Figure S2. This analysis compares the XRD patterns of the two monometallic samples (Pt_0Au_{100} and $Pt_{100}Au_0$) to the bimetallic $Pt_{80}Au_{20}$ material. Scherrer analysis of the XRD data demonstrated that the crystallite sizes of the samples ranged from 3.0 to 2.2 nm (Supporting Information, Table S2). Therefore, the TEM-measured sizes, found to be in agreement with the XRD-determined sizes, are statistically representative of the entire sample. Note that diffraction peaks arising from NaCl were also observed in the sample, which arise from the salts used for the reaction. For the Pt_0Au_{100} peptide-capped NPs, diffraction peaks at 38.4, 44.3, 64.7, and 77.8°2θ were evident, arising from the (111), (200), (220), and (311) diffraction peaks of Au, respectively. Conversely, fewer peaks were evident for the Pt monometallic system ($Pt_{100}Au_0$) with the most prominent Pt-based diffraction being observed at 39.9°2θ for the Pt(111) diffraction. For the bimetallic $Pt_{80}Au_{20}$ peptide-passivated particles, the (111) diffraction peak was at 39.1°2θ, which is positioned directly between the (111) diffraction peaks of Au and Pt. This suggests that the BNPs do contain a mixture of the two metals; however, the arrangement of Pt and Au in the sample cannot be distinguished. ICP−MS analysis was conducted on an Agilent 7900 inductively coupled plasma mass spectrometer.

FEFF and FDMNES Simulations. For the NN-assisted XANES analysis, we followed similar approaches as described in the previous work on the monometallic,[14,15] bimetallic,[16,17] metal oxide systems.[18] XANES simulations utilized two ab initio codes: FEFF[33] and FDMNES.[34] For FEFF simulation, FEFF version 9.6.4 was used for self-consistent calculation within full multiple scattering (FMS) and muffin-tin (MT) approximations. The cluster of a radius of 5.5 Å was used for self-consistent calculation and a cluster of a radius of 7 Å for FMS calculations. S_0^2 was optimized as the 0.9 Au L_3-edge. The random phase approximation was used to model the core-hole, as well as complex exchange-correlation Hedin−Lundqvist potential. For the FDMENS simulation, we used the FDMNES II program, revision 9. The FMS and MT approximations were applied, and the real Hedin−Lundqvist exchange-correlation potential was used for the simulation. The parameters for the simulation were optimized based on the overlap between the experimental and theoretical XANES on the Au and Pt

https://doi.org/10.1021/acsanm.2c00393
ACS Appl. Nano Mater. 2022, 5, 8775−8782

foils, as shown in Figure S3. To show the sensitivity of XANES to the compositional effect, different ratios of Au/Pt of the BNPs are simulated in FEFF, as shown in Figure S4. For the training dataset construction, all the models utilized in our simulation were based on a previous work, where the (100) and (111) lattice planes are utilized to cut the bulk and obtain the models with different sizes and shapes.[14] The ratios of Au/Pt were varied from 9:1 to 1:9, and the site of Au and Pt was randomly assigned. The nonequivalent sites in all cluster models were selected for XANES calculation. All theoretical XANES spectra were shifted in energy by ΔE to align the energy scale of theoretical calculations with experimental data. The energy range of the Au L_3-edge was from 11,910 to 11,973 eV. The energy range of the Pt L_3-edge was from 11,562 to 11,642 eV. To maximize the variability and increase the size of the dataset, linear combinations of randomly selected site-specific XANES, based on the equations of $\mu(E) = \sum_{j=1}^{n}\mu_j/n$, were utilized to enlarge the XANES-CN datasets, where n is optimized to 3 according to the NN performance. Then, we randomly selected three XANES-CN pairs from our original site-specific dataset to create 100,000 spectra. For the NN training, the data were split in 8:1:1 as training, validation, and test datasets, respectively. The architecture of the NN is described in Table S1. We used mean squared loss as the metric to evaluate our NN model and "ADAM" as our optimization algorithm with default parameters ($\beta 1 = 0.9$ and $\beta 2 = 0.99$). To overcome the overfitting, the L2 regularization term was utilized with a 0.001 value. The batch size was optimized to 800 for our NN models.

■ ASSOCIATED CONTENT

Supporting Information

The Supporting Information is available free of charge at https://pubs.acs.org/doi/10.1021/acsanm.2c00393.

AuPt NP synthesis; UV−vis analysis of the AuPt NPs during the synthesis; STEM, HAADF−STEM, XRD, and EDS mapping analysis of the AuPt NPs; FEFF and FDMNES simulations of the AuPt NPs; and error estimation based on the theoretical validation (PDF)

■ AUTHOR INFORMATION

Corresponding Authors

Marc R. Knecht − *Department of Chemistry, University of Miami, Coral Gables, Florida 33146, United States; Dr. J.T. Macdonald Foundation Biomedical Nanotechnology Institute, University of Miami, Miami, Florida 33136, United States;* orcid.org/0000-0002-7614-7258; Email: anatoly.frenkel@stonybrook.edu

Anatoly I. Frenkel − *Department of Materials Science and Chemical Engineering, Stony Brook University, Stony Brook, New York 11794, United States; Chemistry Division, Brookhaven National Laboratory, Upton, New York 11973, United States;* orcid.org/0000-0002-5451-1207; Email: knecht@miami.edu

Authors

Yang Liu − *Department of Materials Science and Chemical Engineering, Stony Brook University, Stony Brook, New York 11794, United States;* orcid.org/0000-0003-4347-1729

Maichong Xie − *Department of Chemistry, University of Miami, Coral Gables, Florida 33146, United States;* orcid.org/0000-0002-1654-952X

Nicholas Marcella − *Department of Materials Science and Chemical Engineering, Stony Brook University, Stony Brook, New York 11794, United States*

Alexandre C. Foucher − *Department of Materials Science and Engineering, University of Pennsylvania, Philadelphia, Pennsylvania 19104, United States;* orcid.org/0000-0001-5042-4002

Eric A. Stach − *Department of Materials Science and Engineering, University of Pennsylvania, Philadelphia, Pennsylvania 19104, United States;* orcid.org/0000-0002-3366-2153

Complete contact information is available at: https://pubs.acs.org/10.1021/acsanm.2c00393

Author Contributions

#Y.L. and M.X. contributed equally.

Notes

The authors declare no competing financial interest.

■ ACKNOWLEDGMENTS

This contribution has been primarily supported by the National Science Foundation under grants 1903576 (A.I.F.) and 1903649 (M.R.K.). Electron microscopy analysis by A.C.F. and E.A.S. was supported as part of the Integrated Mesoscale Architectures for Sustainable Catalysis (IMASC), an Energy Frontier Research Center funded by the U.S. Department of Energy (DOE), Office of Science, Basic Energy Sciences under award #DE-SC0012573. This research used beamline 8-ID of the National Synchrotron Light Source II, a U.S. DOE Office of Science User Facility operated for the DOE Office of Science by the Brookhaven National Laboratory under contract no. DE-SC0012704. This research used resources of the Center for Functional Nanomaterials, which is a U.S. DOE Office of Science Facility, and the Scientific Data and Computing Center, a component of the Computational Science Initiative, at the Brookhaven National Laboratory under contract no. DE-SC0012704. This work was carried out in part at the Singh Center for Nanotechnology at the University of Pennsylvania, which is supported by the NSF National Nanotechnology Coordinated Infrastructure Program under grant NNCI-2025608. Additional support to the Nanoscale Characterization Facility at the Singh Center has been provided by the Laboratory for Research on the Structure of Matter (MRSEC) supported by the National Science Foundation (DMR-1720530). We thank E. Stavitski and D. Leshchev for synchrotron measurements.

■ REFERENCES

(1) Loza, K.; Heggen, M.; Epple, M. Synthesis, Structure, Properties, and Applications of Bimetallic Nanoparticles of Noble Metals. *Adv. Funct. Mater.* **2020**, *30*, 1909260.

(2) Ferrer, D.; Torres-Castro, A.; Gao, X.; Sepúlveda-Guzmán, S.; Ortiz-Méndez, U.; José-Yacamán, M. Three-Layer Core/Shell Structure in Au−Pd Bimetallic Nanoparticles. *Nano Lett.* **2007**, *7*, 1701−1705.

(3) Alayoglu, S.; Zavalij, P.; Eichhorn, B.; Wang, Q.; Frenkel, A. I.; Chupas, P. Structural and Architectural Evaluation of Bimetallic Nanoparticles: A Case Study of Pt−Ru Core−Shell and Alloy Nanoparticles. *ACS Nano* **2009**, *3*, 3127−3137.

(4) Yu, W.; Porosoff, M. D.; Chen, J. G. Review of Pt-Based Bimetallic Catalysis: From Model Surfaces to Supported Catalysts. *Chem. Rev.* **2012**, *112*, 5780−5817.

(5) Zhang, J.; Sasaki, K.; Sutter, E.; Adzic, R. R. Stabilization of Platinum Oxygen-Reduction Electrocatalysts Using Gold Clusters. *Science* **2007**, *315*, 220−222.

(6) Chen, T.; Rodionov, V. O. Controllable Catalysis with Nanoparticles: Bimetallic Alloy Systems and Surface Adsorbates. *ACS Catal.* **2016**, *6*, 4025−4033.

(7) Göltl, F.; Müller, P.; Uchupalanun, P.; Sautet, P.; Hermans, I. Developing a Descriptor-Based Approach for CO and NO Adsorption Strength to Transition Metal Sites in Zeolites. *Chem. Mater.* **2017**, *29*, 6434−6444.

(8) Ghiringhelli, L. M.; Vybiral, J.; Ahmetcik, E.; Ouyang, R.; Levchenko, S. V.; Draxl, C.; Scheffler, M. Learning physical descriptors for materials science by compressed sensing. *New J. Phys.* **2017**, *19*, 023017.
(9) Frenkel, A. I. Applications of extended X-ray absorption fine-structure spectroscopy to studies of bimetallic nanoparticle catalysts. *Chem. Soc. Rev.* **2012**, *41*, 8163−8178.
(10) Hwang, B.-J.; Sarma, L. S.; Chen, J.-M.; Chen, C.-H.; Shih, S.-C.; Wang, G.-R.; Liu, D.-G.; Lee, J.-F.; Tang, M.-T. Structural Models and Atomic Distribution of Bimetallic Nanoparticles as Investigated by X-ray Absorption Spectroscopy. *J. Am. Chem. Soc.* **2005**, *127*, 11140−11145.
(11) Menard, L. D.; Wang, Q.; Kang, J. H.; Sealey, A. J.; Girolami, G. S.; Teng, X.; Frenkel, A. I.; Nuzzo, R. G. Structural characterization of bimetallic nanomaterials with overlapping x-ray absorption edges. *Phys. Rev. B: Condens. Matter Mater. Phys.* **2009**, *80*, 064111.
(12) Liu, J.; Amit, Y.; Li, Y.; Plonka, A. M.; Ghose, S.; Zhang, L.; Stach, E. A.; Banin, U.; Frenkel, A. I. Reversed Nanoscale Kirkendall Effect in Au−InAs Hybrid Nanoparticles. *Chem. Mater.* **2016**, *28*, 8032−8043.
(13) Frenkel, A. I.; Wang, Q.; Sanchez, S. I.; Small, M. W.; Nuzzo, R. G. Short range order in bimetallic nanoalloys: An extended X-ray absorption fine structure study. *J. Chem. Phys.* **2013**, *138*, 064202.
(14) Timoshenko, J.; Lu, D.; Lin, Y.; Frenkel, A. I. Supervised Machine-Learning-Based Determination of Three-Dimensional Structure of Metallic Nanoparticles. *J. Phys. Chem. Lett.* **2017**, *8*, 5091−5098.
(15) Dias, E. T.; Gill, S. K.; Liu, Y.; Halstenberg, P.; Dai, S.; Huang, J.; Mausz, J.; Gakhar, R.; Phillips, W. C.; Mahurin, S.; Pimblott, S. M.; Wishart, J. F.; Frenkel, A. I. Radiation-Assisted Formation of Metal Nanoparticles in Molten Salts. *J. Phys. Chem. Lett.* **2021**, *12*, 157−164.
(16) Marcella, N.; Liu, Y.; Timoshenko, J.; Guan, E.; Luneau, M.; Shirman, T.; Plonka, A. M.; van der Hoeven, J. E. S.; Aizenberg, J.; Friend, C. M.; Frenkel, A. I. Neural network assisted analysis of bimetallic nanocatalysts using X-ray absorption near edge structure spectroscopy. *Phys. Chem. Chem. Phys.* **2020**, *22*, 18902−18910.
(17) Liu, Y.; Halder, A.; Seifert, S.; Marcella, N.; Vajda, S.; Frenkel, A. I. Probing Active Sites in CuxPdy Cluster Catalysts by Machine-Learning-Assisted X-ray Absorption Spectroscopy. *ACS Appl. Mater. Interfaces* **2021**, *13*, 53363−53374.
(18) Liu, Y.; Marcella, N.; Timoshenko, J.; Halder, A.; Yang, B.; Kolipaka, L.; Pellin, M. J.; Seifert, S.; Vajda, S.; Liu, P.; Frenkel, A. I. Mapping XANES spectra on structural descriptors of copper oxide clusters using supervised machine learning. *J. Chem. Phys.* **2019**, *151*, 164201.
(19) Carbone, M. R.; Topsakal, M.; Lu, D.; Yoo, S. Machine-Learning X-Ray Absorption Spectra to Quantitative Accuracy. *Phys. Rev. Lett.* **2020**, *124*, 156401.
(20) Chen, Z.; Andrejevic, N.; Drucker, N. C.; Nguyen, T.; Xian, R. P.; Smidt, T.; Wang, Y.; Ernstorfer, R.; Tennant, D. A.; Chan, M.; Li, M. Machine learning on neutron and x-ray scattering and spectroscopies. *Chem. Phys. Rev.* **2021**, *2*, 031301.
(21) Zheng, C.; Mathew, K.; Chen, C.; Chen, Y.; Tang, H.; Dozier, A.; Kas, J. J.; Vila, F. D.; Rehr, J. J.; Piper, L. F. J.; Persson, K. A.; Ong, S. P. Automated generation and ensemble-learned matching of X-ray absorption spectra. *npj Comput. Mater.* **2018**, *4*, 12.
(22) Zhao, Y.; Ye, C.; Liu, W.; Chen, R.; Jiang, X. Tuning the Composition of AuPt Bimetallic Nanoparticles for Antibacterial Application. *Angew. Chem., Int. Ed.* **2014**, *53*, 8127−8131.
(23) López-Estrada, O.; Zuniga-Gutierrez, B.; Selenius, E.; Malola, S.; Häkkinen, H. Magnetically induced currents and aromaticity in ligand-stabilized Au and AuPt superatoms. *Nat. Commun.* **2021**, *12*, 2477.
(24) Hnilova, M.; Oren, E. E.; Seker, U. O. S.; Wilson, B. R.; Collino, S.; Evans, J. S.; Tamerler, C.; Sarikaya, M. Effect of Molecular Conformations on the Adsorption Behavior of Gold-Binding Peptides. *Langmuir* **2008**, *24*, 12440−12445.
(25) Elding, L. I.; Olsson, L. F. Electronic absorption spectra of square-planar chloro-aqua and bromo-aqua complexes of palladium(II) and platinum(II). *J. Phys. Chem.* **1978**, *82*, 69−74.
(26) Knecht, M. R.; Weir, M. G.; Myers, V. S.; Pyrz, W. D.; Ye, H.; Petkov, V.; Buttrey, D. J.; Frenkel, A. I.; Crooks, R. M. Synthesis and Characterization of Pt Dendrimer-Encapsulated Nanoparticles: Effect of the Template on Nanoparticle Formation. *Chem. Mater.* **2008**, *20*, 5218−5228.
(27) Munro, C. J.; Knecht, M. R. Solution Effects on Peptide-Mediated Reduction and Stabilization of Au Nanoparticles. *Langmuir* **2017**, *33*, 13757−13765.
(28) Si, S.; Mandal, T. K. Tryptophan-Based Peptides to Synthesize Gold and Silver Nanoparticles: A Mechanistic and Kinetic Study. *Chem.—Eur. J.* **2007**, *13*, 3160−3168.
(29) Selvakannan, P.; Swami, A.; Srisathiyanarayanan, D.; Shirude, P. S.; Pasricha, R.; Mandale, A. B.; Sastry, M. Synthesis of Aqueous Au Core−Ag Shell Nanoparticles Using Tyrosine as a pH-Dependent Reducing Agent and Assembling Phase-Transferred Silver Nanoparticles at the Air−Water Interface. *Langmuir* **2004**, *20*, 7825−7836.
(30) Slocik, J. M.; Naik, R. R.; Stone, M. O.; Wright, D. W. Viral templates for gold nanoparticle synthesis. *J. Mater. Chem.* **2005**, *15*, 749−753.
(31) Tan, Y. N.; Lee, J. Y.; Wang, D. I. C. Uncovering the Design Rules for Peptide Synthesis of Metal Nanoparticles. *J. Am. Chem. Soc.* **2010**, *132*, 5677−5686.
(32) Creighton, J. A.; Eadon, D. G. Ultraviolet−visible absorption spectra of the colloidal metallic elements. *J. Chem. Soc., Faraday Trans.* **1991**, *87*, 3881−3891.
(33) Rehr, J. J.; Kas, J. J.; Vila, F. D.; Prange, M. P.; Jorissen, K. Parameter-free calculations of X-ray spectra with FEFF9. *Phys. Chem. Chem. Phys.* **2010**, *12*, 5503−5513.
(34) Bunău, O.; Joly, Y. Self-consistent aspects of x-ray absorption calculations. *J. Phys.: Condens. Matter* **2009**, *21*, 345501.
(35) Cowley, J. M. Short-Range Order and Long-Range Order Parameters. *Phys. Rev.* **1965**, *138*, A1384−A1389.
(36) Duan, Z.; Timoshenko, J.; Kunal, P.; House, S. D.; Wan, H.; Jarvis, K.; Bonifacio, C.; Yang, J. C.; Crooks, R. M.; Frenkel, A. I.; Humphrey, S. M.; Henkelman, G. Structural characterization of heterogeneous RhAu nanoparticles from a microwave-assisted synthesis. *Nanoscale* **2018**, *10*, 22520−22532.
(37) Foucher, A. C.; Marcella, N.; Lee, J. D.; Tappero, R.; Murray, C. B.; Frenkel, A. I.; Stach, E. A. Dynamical Change of Valence States and Structure in NiCu3 Nanoparticles during Redox Cycling. *J. Phys. Chem. C* **2022**, *126*, 1991−2002.
(38) Guan, E.; Foucher, A. C.; Marcella, N.; Shirman, T.; Luneau, M.; Head, A. R.; Verbart, D. M. A.; Aizenberg, J.; Friend, C. M.; Stacchiola, D.; Stach, E. A.; Frenkel, A. I. New Role of Pd Hydride as a Sensor of Surface Pd Distributions in Pd−Au Catalysts. *ChemCatChem* **2019**, *12*, 717−721.
(39) Li, Y.; Zakharov, D.; Zhao, S.; Tappero, R.; Jung, U.; Elsen, A.; Baumann, P.; Nuzzo, R. G.; Stach, E. A.; Frenkel, A. I. Complex structural dynamics of nanocatalysts revealed in Operando conditions by correlated imaging and spectroscopy probes. *Nat. Commun.* **2015**, *6*, 7583.
(40) Sun, Y.; Frenkel, A. I.; Isseroff, R.; Shonbrun, C.; Forman, M.; Shin, K.; Koga, T.; White, H.; Zhang, L.; Zhu, Y.; Rafailovich, M. H.; Sokolov, J. C. Characterization of palladium nanoparticles by using X-ray reflectivity, EXAFS, and electron microscopy. *Langmuir* **2006**, *22*, 807−816.
(41) Zhao, S.; Li, Y.; Liu, D.; Liu, J.; Liu, Y.-M.; Zakharov, D. N.; Wu, Q.; Orlov, A.; Gewirth, A. A.; Stach, E. A.; Nuzzo, R. G.; Frenkel, A. I. Multimodal Study of the Speciations and Activities of Supported Pd Catalysts During the Hydrogenation of Ethylene. *J. Phys. Chem. C* **2017**, *121*, 18962−18972.
(42) Choi, H. C.; Shim, M.; Bangsaruntip, S.; Dai, H. Spontaneous Reduction of Metal Ions on the Sidewalls of Carbon Nanotubes. *J. Am. Chem. Soc.* **2002**, *124*, 9058−9059.

https://doi.org/10.1021/acsanm.2c00393
ACS Appl. Nano Mater. 2022, 5, 8775−8782